A SnO_2 Nanoparticle/Nanobelt and Si Heterojunction Light-Emitting Diode

Bo Ling,[†] Xiao Wei Sun,*[,†,‡] Jun Liang Zhao,[†,‡] Chang Ke,[†] Swee Tiam Tan,[†] Rui Chen,[§] Han Dong Sun,[§] and Zhi Li Dong[||]

School of Electrical and Electronic Engineering, Nanyang Technological University, 50 Nanyang Avenue, 639798, Singapore, Department of Applied Physics, College of Science, Tianjin University, 92 Weijin Road, Tianjin 300072, P. R. China, Division of Physics and Applied Physics, School of Physical and Mathematical Sciences, Nanyang Technological University, 21 Nanyang Link, 637371, Singapore, and School of Materials Science and Engineering, Nanyang Technological University, 50 Nanyang Avenue, 639798, Singapore

Received: July 17, 2010; Revised Manuscript Received: October 4, 2010

Single-crystalline zero-dimensional tin dioxide (SnO_2) nanoparticles and one-dimensional SnO_2 nanobelts were synthesized on silicon (Si) substrates with different seed layer coatings by simple vapor-phase transport method. The crystal structure and morphology of the as-synthesized products were characterized by X-ray diffraction, scanning electron microscopy, transmission electron microscopy, and Raman scattering spectroscopy. Both geometrically different nanostructures were further employed to fabricate the light-emitting diodes and showed dominant red and green emission bands at room temperature, which were ascribed to the deep defect states in SnO_2. However, SnO_2-nanobelts-based light-emitting diodes showed another violet emission peaking at ca. 400 nm which was attributed to the shallow defect state related to the surface states/defects. The different emission performance between nanoparticle and nanobelts devices was attributed to the larger surface-to-volume ratio of the nanobelts, which was confirmed by the Raman and photoluminescence analysis. A thin SiO_2 intermediate layer was found to be crucial in achieving light emission from a n-SnO_2/p-Si heterojunction with large valence band offset (ca. 2.96 eV), by which sufficient potential-energy difference can be maintained between SnO_2 and Si, thus facilitating the tunneling injection of holes.

1. Introduction

Tin dioxide (SnO_2, stannic tin oxide) is an interesting semiconductor system because of its dipole-forbidden direct band gap of 3.6 eV at room temperature (RT).[1] It has been widely studied and regarded as one of the most promising materials for transparent electrodes,[2] gas sensors,[3] solar cells,[4] and field-effect transistors.[5] Although SnO_2 has a large exciton binding energy of 130 meV, which promises efficient exciton emission at RT and even at higher temperatures, the optoelectronic devices based on the bulk SnO_2 are highly underdeveloped because of its dipole-forbidden nature as well as the poor crystallinity of the materials fabricated.[6] Recently, the advance in fabrication of nanostructured SnO_2 has attracted new interest in exploiting this material as components for nanoscale light emitters because the dipole-forbidden selection rule may fail because of the breaking of the wave-function symmetry in low-dimensional systems. Different morphologies of SnO_2 nanostructures such as nanoparticles (NPs), nanowires (NWs)/nanorods (NRs), nanobelts (NBs)/nanoribbons, and nanotubes have been fabricated by various methods including vapor-phase transport method, solution method, sol−gel method, and so forth.[7−11] Photoluminescence (PL) characterization was widely employed to investigate the optical properties of these SnO_2 nanostructures. It was demonstrated that nanostructured SnO_2 usually showed a strong broadband emission (380−640 nm) at RT which was always attributed to different defect trapped states in the SnO_2 band gap, whereas bulk SnO_2 generally showed no or very low-intensity luminescence.[12−15] Hitherto, however, few research groups have reported the electroluminescence (EL) performance from nanostructured-SnO_2-based LEDs. Only very recently, SnO_2 began to manifest its practical application in light-emitting devices. In 2008, RT EL emission from an n-SnO_2 polycrystalline film/p-Si heterojunction was reported where the SnO_2 film surface was modified to a wormlike nanostructure.[6] Later on, EL from SnO_2 NWs/NRs on both p-SiC and p-GaN:Mg substrates was observed.[16,17]

In this paper, we reported RT EL emissions from randomly packed SnO_2 NPs and NBs directly grown on p-Si substrates with morphology controlled by the seed layer, which is an ideal system for fabricating low-cost LEDs. The different EL performances from these two kinds of LEDs are discussed, and the emission mechanism is illustrated by means of the energy-band diagram.

2. Experimental Section

2.1. Substrate Preparation. Before deposition, p-Si(100) substrates (0.01−0.02 ohm cm) were ultrasonically cleaned by acetone, isopropyl alcohol (IPA), and deionized (DI) water sequentially, each for 15 min, and finally dried under N_2-gas flow. After that, we prepared two different seed layers on the Si substrates by using dc magnetron sputtering (Au seed layer) and metal−organic chemical vapor deposition (MOCVD, SnO_2 seed layer), respectively. The Au layer was deposited on the Si substrates in Ar gas under the working pressure of 5×10^{-4} Torr with a power of 60−70 W at RT. The thickness of the Au layer was controlled by the sputtering time, and ca. 8 nm Au was deposited on the Si substrates, measured by a surface

* To whom correspondence should be addressed. E-mail: exwsun@ntu.edu.sg.
[†] School of Electrical and Electronic Engineering, Nanyang Technological University.
[‡] Tianjin University.
[§] School of Physical and Mathematical Sciences, Nanyang Technological University.
[||] School of Materials Science and Engineering, Nanyang Technological University.

10.1021/jp106650p © 2010 American Chemical Society
Published on Web 10/12/2010

profiler (Tencor P-10). Another SnO_2 film seed layer (ca. 80 nm) prepared by MOCVD technique was grown on Si substrates at 450 °C with a chamber pressure of 25 Torr and by using Tetraethyltin (TESn) and O_2 as the precursors.

2.2. Nanostructure Growth. Our synthesis is based on thermal evaporation of Sn metal powders (99.9%, 45 μm, Goodfellow) under 750 °C by the vapor-phase transport (VPT) method.[18] The Sn powder was placed in an alumina boat and covered with several pieces of Si wafers (the perpendicular distance between the substrates and powder was ca. 5 mm). The boat was positioned in a small quartz tube which was then inserted into a horizontal tube furnace, where the temperature, pressure, and evaporation time were well controlled. Two kinds of Si substrates with different seed layer coatings (Au and SnO_2) were employed to direct the growth of SnO_2 nanostructures. During the synthesis, the evaporation temperature was kept at 750 °C, and the chamber pressure was maintained at ca. 2 Torr under O_2- and Ar-gas flow (with a volume ratio of ca. 2%). After evaporation during 1 h, large quantities of white products were formed on the surface of the Au- and SnO_2-coated Si substrates.

2.3. Device Fabrication. A bilayer Ti (5 nm)/Au (15 nm) cathode was directly fabricated on the SnO_2 NPs and NBs as an ohmic contact by electron-beam (e-beam) evaporation method.[19] On the other hand, a Au anode ca. 100 nm thick was deposited on the back side of Si wafers by dc magnetron sputtering. It is worth pointing out that the backside of the p-Si wafers were etched by 2% hydrofluoric acid (HF) solution to remove the native oxide before fabricating the Au anode. The whole devices were then annealed at 300 °C for 1 min in air to improve the contact performance.

2.4. Characterization. The crystal structure and morphology of the products were characterized and analyzed by X-ray diffraction (XRD, Siemens D5005 X-ray diffractometer with Cu $K_{\alpha 1}$ radiation), scanning electron microscopy (SEM, JEOL JSM-5910LV), transmission electron microscopy (TEM, JEM-2010 operated at 200 kV), and Raman scattering spectrum (Renishaw Ramanscope with an Ar^+ laser operating at 514.5 nm as the excitation source and a resolution of ca. 1 cm^{-1}). The luminescence properties of the two kinds of LEDs were investigated by PL (He−Cd laser with 325 nm line as the excitation source) and EL spectra. All the characterizations were conducted at RT.

To prepare the NP and NB samples for TEM characterization, the as-synthesized nanostructures were first carefully scrapped from the substrates and then dispersed into ethanol by ultra-sonication. Several drops of the solutions were dripped onto the carbon-coated copper grids. After drying, the sample is ready for characterization.

3. Results and Discussion

The structure of the as-synthesized nanostructures was determined by XRD as shown in Figure 1a. It was found that the morphology of the products can be tuned by the seed layer. NPs were found to be grown on SnO_2-coated Si substrates, whereas NBs were formed on the Au-coated Si substrates. All the diffraction peaks in NP and NB samples can be well indexed into the tetragonal rutile SnO_2 structure with lattice constants of $a = 4.738$ Å and $c = 3.187$ Å (JCPDS card No. 41−1445). An additional broad peak located at ca. 44.4° in SnO_2 NB sample was assigned to Au (200) (JCPDS card No. 04−0784). Figure 1b,c is the typical SEM images of the as-grown SnO_2 NPs and NBs, respectively. NP samples were found randomly packed on the Si substrate forming a ca. 2 μm thick layer and

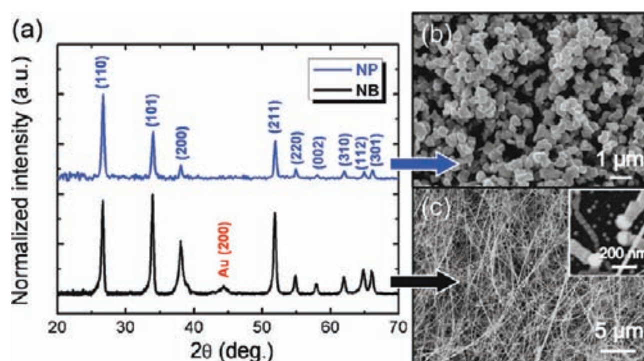

Figure 1. (a) XRD patterns of randomly packed SnO_2 NPs and NBs grown on SnO_2- and Au-coated Si substrates, respectively. Low-magnification SEM images of as-synthesized (b) SnO_2 NPs and (c) SnO_2 NBs. Inset in panel c is the enlarged SEM image of SnO_2 NBs with Au particle at the NB growth tip with growth time of 5 min for a clear view, which indicates the typical VLS growth mechanism.

showed a broad size distribution in the range from 300 nm up to 1 μm. The widths of the entangled NB samples are mainly in the range of 40−100 nm with a thickness of several tens of nanometers and a length up to several hundred micrometers. A ca. 5 μm thick NB layer was formed on the Au-coated Si substrates after synthesis for 1 h. As seen from the enlarged SEM image at the NB tip [inset in Figure 1c], the vapor-liquid-solid (VLS) mechanism is confirmed to account for the NB growth, which is consistent with the XRD result.[20,21] On the contrary, the growth of SnO_2 NPs should be dominated by the vapor-solid (VS) mechanism in which SnO_2 seed layer behaves as a preferential nucleation site.[22]

The crystal structure of the as-synthesized NPs and NBs was further investigated by TEM characterization. The characteristic shape of the SnO_2 NPs is displayed in Figure 2a. NPs with different sizes were aggregated together and possessed a rutile tetragonal crystal structure, confirmed from the corresponding selected area electron diffraction (SAED) pattern shown in Figure 2b. The bend contour patterns can be seen from the SnO_2 NB sample with the typical width of ca. 40 nm shown in Figure 2c. The white arrowhead indicates the growth direction of the NB. A high-resolution TEM (HRTEM) image [Figure 2d] reveals that the NB is single-crystal nature with few dislocations and defects. The lattice spacings of 2.6 and 2.3 Å correspond to the distances between the (101)/(10$\bar{1}$) and (200) planes of SnO_2, respectively. The measured angles between the (101) and (10$\bar{1}$) planes (marked by double arrows) are consistent with the values in tetragonal rutile SnO_2 structure.[23] The corresponding SAED pattern [Figure 2e] recorded along the [010]-zone axis further confirms that the as-grown SnO_2 NB is of single-crystal nature with a tetragonal rutile phase and indicates that the NB grows along the [101] direction.

As a useful tool for the characterization of nanosized materials and a qualitative probe of the presence of lattice defects in solids, Raman scattering was employed to investigate the as-synthesized SnO_2 nanostructures.[24] Figure 3a,b shows the Raman spectra of the SnO_2 NPs and NBs, respectively. Three fundamental Raman scattering peaks (E_g, A_{1g}, and B_{2g}) in both samples showed the typical feature of the rutile SnO_2,[24] which is consistent with the XRD results. The peak at ca. 522 cm^{-1} corresponds to the TO vibration mode of the single-crystal Si. It is known that A_{1g} and B_{2g} are nondegenerate normal phonon modes which vibrate in the plane perpendicular to the c-axis and are related to the expansion and contraction vibration of Sn−O bonds, respectively. The doubly degenerated E_g mode

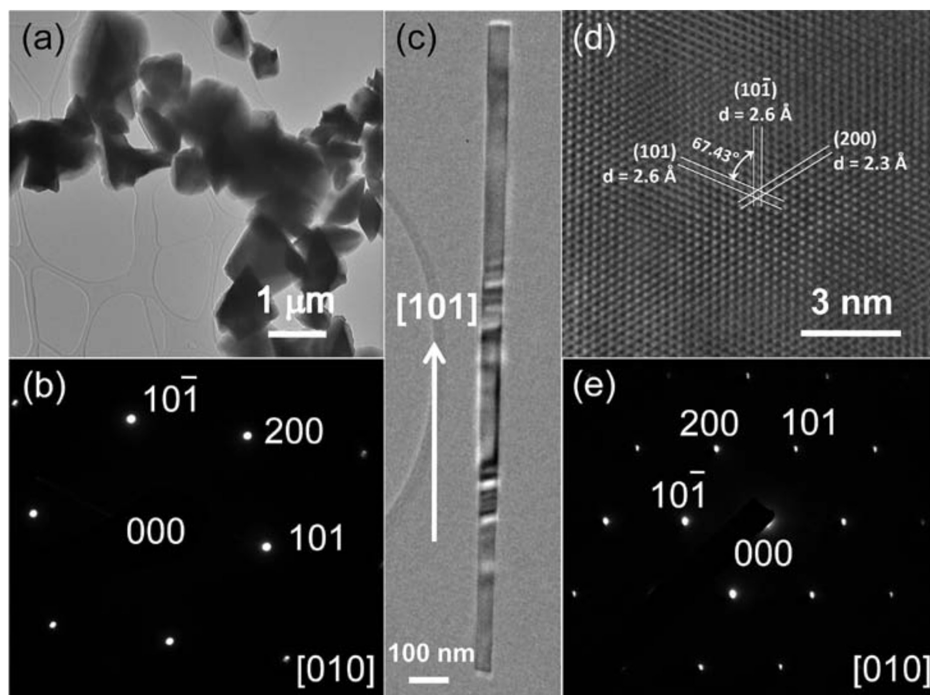

Figure 2. TEM image of (a) the SnO_2 NP sample and (b) the corresponding SAED pattern taken along the [010]-zone axis. (c) Low-magnification and (d) high-resolution TEM images of the SnO_2 NB sample with (e) the corresponding SAED pattern taken along the [010]-zone axis. The white arrowhead in panel c shows that the growth direction of the SnO_2 NB is along the [101] direction.

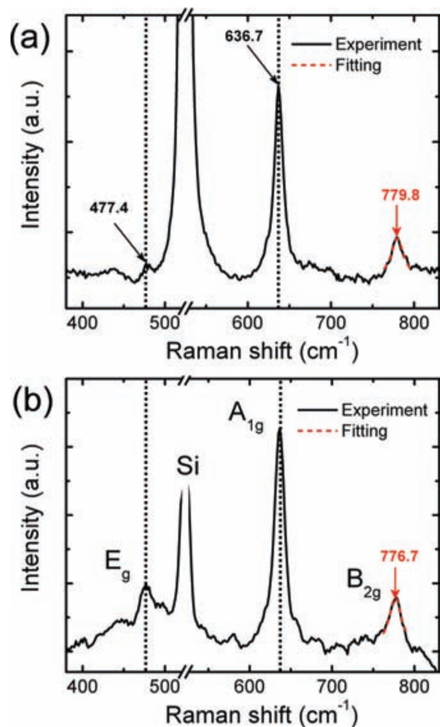

Figure 3. Raman scattering spectra of SnO_2 (a) NP and (b) NB samples. Red short-dashed lines show the Lorentzian fitting of the B_{2g} peak.

represents two oxygen atoms vibrating out of phase along the c-axis.[25] According to the phonon dispersion curves, A_{1g} and B_{2g} modes shift toward lower wave numbers as the particle size decreases, whereas mode E_g shifts toward higher wave numbers.[24] From Diéguez's experiment, the B_{2g} mode shows the largest shift compared to the other modes with the decrease of the SnO_2 NP size, whereas the E_g mode is almost immobile.[24] In our experiments, the B_{2g} mode in the SnO_2 NB samples (776.7 cm^{-1}) showed a slight shift to the lower wavenumber compared to that of the SnO_2 NP samples (779.8 cm^{-1}) via Lorentzian fitting, which may be due to the higher surface-to-volume ratio of the NB samples. From our SEM data, the average size of NPs can be taken as 0.5 μm, and the average width, thickness, and length of NBs are 80 nm, 30 nm, and 200 μm, respectively. We assume that the shapes of these two samples are cubic and cuboid, respectively; thus, the surface-to-volume ratios are 12 and 92 μm^{-1}, respectively. However, E_g and A_{1g} vibration modes in both samples appeared at exactly the same positions in the Raman spectra, which are respectively located at 477.4 and 636.7 cm^{-1}. It should be noted that only the shift of the B_{2g} mode is prominent within the detection limit after we compared more than 20 samples, suggesting that B_{2g} may be the most sensitive mode to the size or surface states of SnO_2 nanostructures. In our study, however, the positions of the E_g and A_{1g} vibration modes were found to be independent of the size and morphology of SnO_2 nanostructures.

Figure 4a shows the PL spectra of both SnO_2 NP and NB samples at RT. The broad peaks from 380 to 800 nm observed in both samples are similar to those reported for bulk and nanostructured SnO_2 previously, which is ascribed to the defect energy levels formed in the SnO_2 band gap. Compared with the NP samples, all the SnO_2 NB samples presented a more obvious emission peak centered at ca. 400 nm. To further investigate the emission properties of the SnO_2 NB samples, the PL spectrum was deconvoluted to three Gaussian-shaped peaks as shown in Figure 4b. Three emission peaks are located at 400 nm (3.1 eV), 560 nm (2.2 eV), and 620 nm (2 eV), which indicates that there probably exist three main defect-related radiative recombination centers inside the SnO_2 NBs.[16] The current−voltage ($I-V$) characteristics of these two devices are shown in Figure 4c. The device was forward-biased with the positive voltage applied on the p-Si. Rectifying behavior can be seen from both NP and NB devices with the turn-on voltage at ca. 5 and 5.6 eV, respectively. As seen from the inset

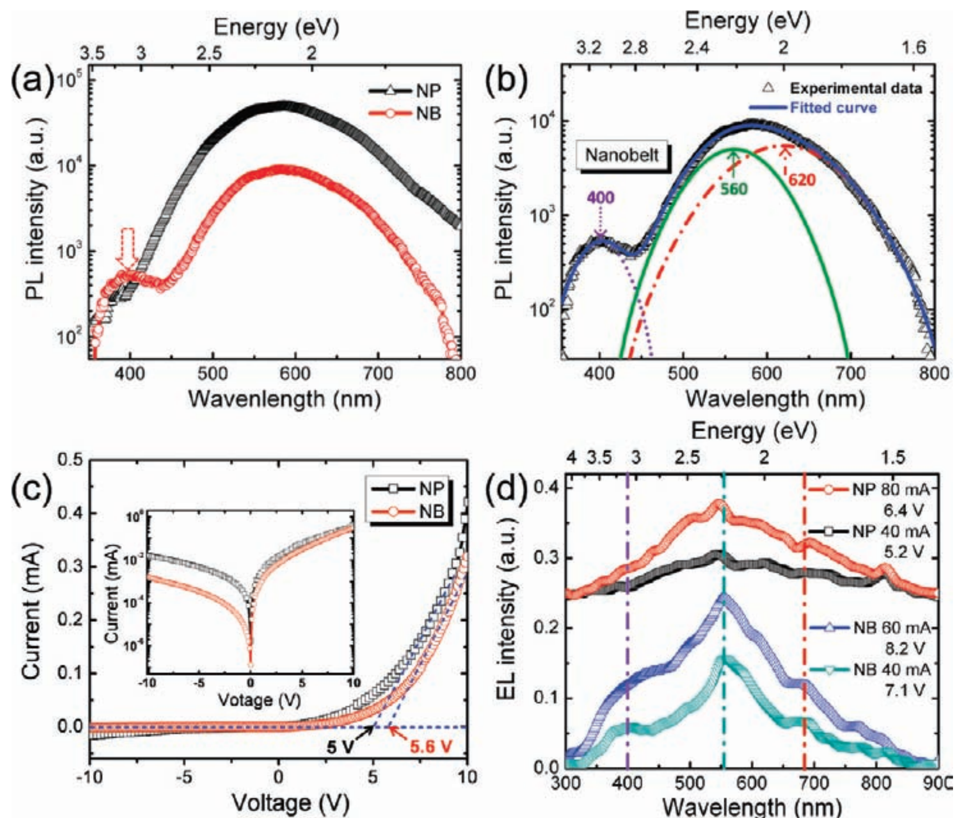

Figure 4. (a) RT PL spectra of SnO_2 NP and NB samples. (b) Fitting results of the SnO_2 NB PL spectra at RT with peak wavelengths at approximately 400 nm (3.1 eV), 560 nm (2.2 eV), and 620 nm (2 eV). (c) Current−voltage characteristics of these two LEDs based on SnO_2 NPs and NBs. The inset shows the same data in semilogarithmic scale. (d) RT EL spectra of both kinds of samples under different forward current injections.

semilogarithmic plot, the on−off ratios at ±10 V in NP and NB devices are ca. 27 and 190, respectively. Figure 4d gives the RT EL spectra of both SnO_2-NP- and SnO_2-NB-based LEDs under different forward current injections. It should be mentioned that the emission light can be clearly observed by the naked eye in a dark environment under forward bias above 4−5 V in both devices. The NP samples showed two main emission peaks at the green (ca. 545 nm) and red (ca. 690 nm) bands, which is similar to the PL spectrum. NB samples also showed the same colored emission bands; however, an additional peak appeared in the violet region at ca. 400 nm which corresponds well with the PL result. On the basis of the PL and EL results, it is indicated that there exist three main defect-related radiative recombination centers formed in the SnO_2 dipole-forbidden band gap which give rise to different emission peaks. The emission peak located in the violet region (ca. 400 nm) in both RT PL and EL spectra is more prominent in the NB samples than in the NP samples. However, the origin of the luminescence peaks and the exact position of defect-related states in SnO_2 are still unclear and controversial because of the strong dependence on the surface states and preparation methods.[14] The discrepant luminescence behavior in these two devices may be related to the morphology and surface-to-volume ratio difference.

It is well known that the crystal size and surface states play an important role in the luminescence behavior of SnO_2 nanostructures.[25] The luminescence in the visible as well as the UV regions has been found to be dependent on the surface states/structures, defects, and impurities.[8] Generally, the green and red/orange emission bands are most commonly observed and coexist in SnO_2 samples, which are both attributed to the deep trapped states forming defect energy levels inside the SnO_2 band gap by defects and/or surface structures.[1,12,25−27] Previously, Yuan et al.[6] suggested that the broad EL emission (500−700 nm) in their SnO_2/p-Si heterojunction was due to the radiative recombination between electrons which were relaxed to the defect states and holes in the valence band (VB). However, the UV-violet emission was generally referred to the radiative recombination between electrons in the shallow trap states and holes in the VB or acceptor levels.[12] It was also reported that UV emissions were due to the weakly bounded excitons at the shallow defect trap states due to the existence of crystalline defects or surface states in SnO_2 NBs and NWs, which would induce localized deformation potential for trapping and dissociation of free excitons.[16,25,28,29]

Figure 5a−c schematically shows the device structure that we applied in the experiment and the surface morphologies of both devices after top cathode layer deposition. It is noted that Ti/Au can form a relatively uniform layer on the SnO_2 NP and NB directly because of the thick tightly packed NPs and NBs, avoiding short circuit by electrode deposition. The inset in Figure 5c shows the SEM image of a NB device surface, the top side of which was intentionally scrapped by a fine-tip tweezer to expose the layer below the cathode for a clear view. This verifies that the deposited cathode layer only forms on the surface of free-standing NBs, which may be due to the shadowing effect of the entangled NBs.

The mechanism of the EL can be further analyzed in terms of the energy-band diagrams based on the Anderson model.[30] What should be mentioned is that a thin SiO_2 layer (ca. 4 nm determined by TEM) was found to be formed on the Si surface. This intermediate layer plays a crucial role in determining the device performance because no light emission can be detected in devices with the SiO_2 layer intentionally removed by HF solution before depositing the seed layers. This suggested that

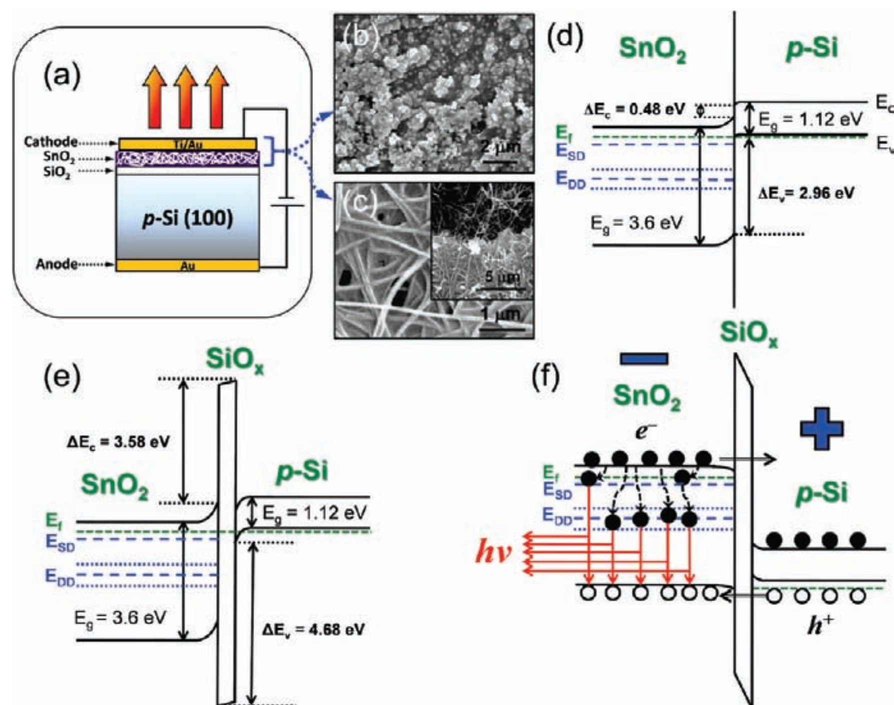

Figure 5. (a) Schematic of the fabricated device structure. Typical top-view SEM images of the (b) NP- and (c) NB-based LEDs after electrode deposition. The top side of the NB sample was carefully scratched by a fine-tip tweezer to expose the inner SnO_2 layer as shown in the inset of panel c, indicating that the Ti/Au contact layer was only formed at the NB surface in our devices. Energy-band diagrams of the heterojunctions made (d) without and (e) with the SiO_2 intermediate layer under zero bias. (f) Energy-band diagram of the n-SnO_2/p-Si heterojunction with the SiO_2 thin layer in between under forward bias. E_f, E_{SD}, and E_{DD} denote the Fermi level, shallow defect-related energy level, and deep defect-related energy level, respectively.

the thin SiO_2 layer between the SnO_2 and Si functioned as a carrier-blocking layer for the LEDs.[31] To simplify the analysis, we neglected the effects of dipole and interfacial states and assumed the continuity of vacuum levels. The electron affinities for SnO_2, Si, and SiO_2 are assumed at 4.53, 4.05, and 0.95 eV, respectively.[6,32] The energy-band gap (E_g) of these three materials are taken as 3.6, 1.12, and 8.9 eV, respectively.[6,16,33] Figure 5d depicts the energy-band diagram of the device made without the SiO_2 layer at the equilibrium. In this case, the barriers for electron and hole injections are 0.48 and 2.96 eV, respectively. The large VB offset between SnO_2 and Si (i.e., $\Delta E_v = 2.96$ eV) makes it impossible to build enough potential at the heterojunction and to inject holes; therefore, no light emission is observed. A similar result was also observed in ZnO NW/p-Si heterojunction without the SiO_2 layer.[34]

On the other hand, by introducing a SiO_2 intermediate layer, both the electron and hole barriers increased and reached 3.58 and 4.68 eV, respectively. Under the zero bias shown in Figure 5e, electrons and holes are well confined at each side and cause the band bending at the SnO_2/SiO_2 and Si/SiO_2 interfaces. When applying appropriate forward bias on the devices, sufficient potential energy difference could be maintained at the SnO_2/Si interface and caused the Fermi level of the Si to move downward and to get closer to the SnO_2 VB. As a result, the accumulated holes in the p-Si side could tunnel through the thin SiO_2 layer into the SnO_2 VB and recombined with the electrons trapped at different energy levels in SnO_2, thus contributing to the different emission bands in the EL spectra. According to previous studies,[6,16] electrons in the SnO_2 conduction band (CB) may first relax to the energy levels of shallow and deep defect states (denoted as E_{SD} and E_{DD}, respectively, in Figure 5), and some portion of electrons trapped in the E_{SD} may further relax to the E_{DD} states. On the basis of our PL and EL results shown above, the violet emission in our NB devices can be attributed to the radiative recombination between the electrons in the shallow trap states with the holes in the VB. As such, the green and red (or orange) emissions are related to electrons trapped in two deep defect states formed in the energy-band gap. It is worth mentioning that there is no EL signal when a positive voltage is applied at the n-SnO_2 side.

4. Conclusions

In summary, we report a facile method to grow single crystalline SnO_2 NPs and NBs directly on p-Si and further fabricated them into heterojunction LEDs. RT EL emissions have been demonstrated from the n-SnO_2 (NPs and NBs)/p-Si heterojunctions. All the emission peaks detected are associated to the presence of different defect states (i.e., shallow and deep defect states) in the SnO_2 band gap, and the luminescence behavior was found to be highly dependent on the morphology of the SnO_2 nanostructures. Green and red/orange emission bands were observed in both SnO_2-NP- and SnO_2-NB-based LEDs, whereas the violet emission (ca. 400 nm) was obvious only in the NB devices. The discrepancy of the EL behavior between these two kinds of devices may be related to the larger surface-to-volume ratio of the NBs than that of the NPs, which was in accord with the shift of the B_{2g} mode in Raman spectra. Therefore, the violet emission is related to the surface states/defects, which was considered to be characteristic of the SnO_2 nanostructures with a high surface-to-volume ratio. The SiO_2 intermediate layer was found to be essential in the EL performance in both devices, because of which a large potential energy difference can be built at the heterojunction interface and thus facilitate the holes to tunnel from the p-Si VB into the n-SnO_2 VB. This further contributed to the RT EL emissions from the heterojunctions under appropriate forward biases via radiative recombination between trapped electrons and holes

in SnO_2. Our work not only verifies the possibility to realize the RT EL emission from dipole-forbidden SnO_2 NPs and NBs by a simple growth and device-fabrication process but also shows a promising way to tune the light emissions from SnO_2 by controlling the morphology of the nanostructures, which may also be applicable to other dipole-forbidden direct band gap metal oxide systems.

Acknowledgment. Supports from Singapore Agency for Science, Technology and Research (A*STAR) Science and Engineering Research Council (SERC) under Grant No. 0921010057 and National Natural Science Foundation of China (NSFC) under Grant Nos. 61006037 and 61076015 are gratefully acknowledged.

References and Notes

(1) Yu, B.; Zhu, C.; Gan, F. *Opt. Mater.* **1997**, *7*, 15–20.
(2) Chopra, K. L.; Major, S.; Pandya, D. K. *Thin Solid Films* **1983**, *102*, 1–46.
(3) Albert, K. J.; Lewis, N. S.; Schauer, C. L.; Sotzing, G. A.; Stitzel, S. E.; Vaid, T. P.; Walt, D. R. *Chem. Rev.* **2000**, *100*, 2595–626.
(4) Hara, K.; Horiguchi, T.; Kinoshita, T.; Sayama, K.; Sugihara, H.; Arakawa, H. *Sol. Energy Mater. Sol. Cells* **2000**, *64*, 115–134.
(5) Arnold, M. S.; Avouris, P.; Pan, Z. W.; Wang, Z. L. *J. Phys. Chem. B* **2003**, *107*, 659–663.
(6) Yuan, Z.; Li, D.; Wang, M.; Chen, P.; Gong, D.; Cheng, P.; Yang, D. *Appl. Phys. Lett.* **2008**, *92* (1−3)), 121908.
(7) Leite, E. R.; Weber, I. T.; Longo, E.; Varela, J. A. *Adv. Mater.* **2000**, *12*, 965–968.
(8) Kar, A.; Stroscio, M. A.; Dutta, M.; Kumari, J.; Meyyappan, M. *Appl. Phys. Lett.* **2009**, *94* (1−3)), 101905.
(9) Pan, Z. W.; Dai, Z. R.; Wang, Z. L. *Science* **2001**, *291*, 1947–1949.
(10) Liu, B.; Zeng, H. C. *J. Phys. Chem. B* **2004**, *108*, 5867–5874.
(11) Lu, F.; Chen, S.; Peng, S. *Catal. Today* **1996**, *30*, 183–188.
(12) Liu, R.; Chen, Y.; Wang, F.; Cao, L.; Pan, A.; Yang, G.; Wang, T.; Zou, B. *Physica E (Amsterdam, Neth.)* **2007**, *39*, 223–229.
(13) Hu, J. Q.; Bando, Y.; Liu, Q. L.; Golberg, D. *Adv. Funct. Mater.* **2003**, *13*, 493–496.
(14) Maestre, D.; Cremades, A.; Piqueras, J. *J. Appl. Phys.* **2004**, *95*, 3027–3030.
(15) Zhou, X. T.; Heigl, F.; Murphy, M. W.; Sham, T. K.; Regier, T.; Coulthard, I.; Blyth, R. I. R. *Appl. Phys. Lett.* **2006**, *89* (1−3), 213109.
(16) Yang, H. Y.; Yu, S. F.; Cheng, C. W.; Tsang, S. H.; Liang, H. K.; Fan, H. J. *Appl. Phys. Lett.* **2009**, *95* (1−3), 201104.
(17) Yang, H. Y.; Yu, S. F.; Liang, H. K.; Lau, S. P.; Pramana, S. S.; Ferraris, C.; Cheng, C. W.; Fan, H. J. *ACS Appl. Mater. Interfaces* **2010**, *2*, 1191–1194.
(18) Ling, B.; Sun, X. W.; Shen, Y. Q.; Dong, Z. L. *Appl. Phys. A: Mater. Sci. Process.* **2010**, *98*, 91–96.
(19) Yang, H. S.; Norton, D. P.; Pearton, S. J.; Ren, F. *Appl. Phys. Lett.* **2005**, *87* (1−3), 212106.
(20) Wagner, R. S.; Ellis, W. C. *Appl. Phys. Lett.* **1964**, *4*, 89–90.
(21) Morales, A. M.; Lieber, C. M. *Science* **1998**, *279*, 208–211.
(22) Yang, P.; Lieber, C. M. *J. Mater. Res.* **1997**, *12*, 2981–2996.
(23) Duan, J.; Gong, J.; Huang, H.; Zhao, X.; Cheng, G.; Yu, Z.-Z.; Yang, S. *Nanotechnology* **2007**, *18* (1−6), 055607.
(24) Diéguez, A.; Romano-Rodríguez, A.; Vilà, A.; Morante, J. R. *J. Appl. Phys.* **2001**, *90*, 1550–1557.
(25) Zhou, W.; Liu, R.; Wan, Q.; Zhang, Q.; Pan, A. L.; Guo, L.; Zou, B. *J. Phys. Chem. C* **2009**, *113*, 1719–1726.
(26) Wang, F.; Zhou, X.; Zhou, J.; Sham, T.-K.; Ding, Z. *J. Phys. Chem. C* **2007**, *111*, 18839–18843.
(27) Fillard, J. P.; de Murcia, M. *Phys. Status Solidi A* **1975**, *30*, 279–287.
(28) Kim, T. W.; Lee, D. U.; Yoon, Y. S. *J. Appl. Phys.* **2000**, *88*, 3759–3761.
(29) Gu, F.; Wang, S. Fen.; Song, C. F.; Lü, M. K.; Qi, Y. X.; Zhou, G. J.; Xu, D.; Yuan, D. R. *Chem. Phys. Lett.* **2003**, *372*, 451–454.
(30) Davies, J. H. *The Physics of Low-Dimensional Semiconductors: An Introduction*; Cambridge University Press: Cambridge, UK, 1997.
(31) Zhao, J. L.; Sun, X. W.; Tan, S. T.; Lo, G. Q.; Kwong, D. L.; Cen, Z. H. *Appl. Phys. Lett.* **2007**, *91* (1−3), 263501.
(32) Pan, C. A.; Ma, T. P. *Appl. Phys. Lett.* **1980**, *37*, 714–716.
(33) Ravindra, N. M.; Narayan, J. *J. Appl. Phys.* **1986**, *60*, 1139–1146.
(34) Zimmler, M. A.; Stichtenoth, D.; Ronning, C.; Yi, W.; Narayanamurti, V.; Voss, T.; Capasso, F. *Nano Lett.* **2008**, *8*, 1695–1699.

JP106650P